Spin dynamics in the pulsed spin locking of nuclear quadrupole resonance

K. L. Sauer*
George Mason University, Fairfax, Virginia 22030, USA

C. A. Klug
Code 6122, Naval Research Laboratory, Washington, D.C. 20375, USA

(Received 9 January 2006; revised manuscript received 4 April 2006; published 9 November 2006)

We theoretically examine the perturbative effects of a series of radio-frequency (rf) pulses, electric field gradient inhomogeneity, and dipole-dipole coupling on the spin dynamics of spin-1 nuclei dominated by the quadrupole interaction. The dipole-dipole coupling is between neighboring spin-1 nuclei with identical nuclear quadrupole resonance frequencies, but the principal axes frames of the electric field gradient at each nucleus are *not* aligned. Such a comprehensive treatment is necessary to determine the optimal sequence of rf pulses which maximizes the echoes in the detection of the substance of interest, for example, an explosive or other contraband material. We confirm our theoretical model using the nitrogen in powder samples of *p*-chloroaniline and sodium nitrite.

DOI: 10.1103/PhysRevB.74.174410 PACS number(s): 76.60.Gv, 82.56.Jn, 76.60.Lz, 75.40.Mg

Nuclear quadrupole resonance (NQR) extends the promise of simple detection of quadrupole nuclei within crystalline samples, since neither an electric nor a magnetic static field needs to be applied.[1] However, because the characteristic NQR frequencies fall within the MHz range, the resulting signals tend to be weak. To increase the sensitivity of NQR detection, radio-frequency (rf) pulses are often applied to the sample in quick succession in order to extend or "lock" the signal in time.[2–7]

One such sequence, known as spin-lock spin-echo (SLSE), was described for nuclear magnetic resonance (NMR) by Ostroff and Waugh[8] and later applied to NQR by Marino and Klainer.[9] This sequence includes an rf preparatory pulse θ_0 which produces the initial signal and ensuing pulses θ, shifted in phase by 90° from the first pulse, which serve to continually refocus the signal. The sequence is written, for N refocusing pulses, as $\theta_{0X}-(\tau-\theta_Y-\tau)_N$, where 2τ is the time between the refocusing pulses. In an attempt to explain Marino and Klainer's experimental results, Cantor and Waugh[10] obtained solutions for the problem of two equivalent, both chemically and crystallographically, spin-1 nuclei under the influence of dipolar coupling and a SLSE sequence. Particulary interesting in Cantor and Waugh's theoretical results is the prediction that there should be selective refocusing of the dipolar coupling depending on the strength of the refocusing pulses. Such selective refocusing is key to determining distances between neighboring nitrogen nuclei through NQR. The major obstacle for demonstrating this fundamental behavior has been the neglect of other effects which also strongly influence the effectiveness of the refocusing pulses, namely the distribution of NQR frequencies due to electric field inhomogeneities and the shift in orientation of the electric field gradient from one spin-1 nucleus to the next. Armed with a description of the full-dynamics occurring during refocusing, we have been able to correctly predict the NQR signal as a function of refocusing pulse strength, including therefore the demonstration of the selective refocusing of the pulses.

In the most general case, including all effects, we show how to calculate the signal numerically, an analytical solution being out of reach. However, we give analytical solutions for special cases where possible, in order to offer intuition into the problem. We will examine the case of the rf field being applied near one of the three possible quadrupole transitions. The results given are easily extended to the other two transitions, while the method applied here can be applied to the analysis of any multiple-pulse sequence in NQR. Our goal is not only to present a consistent theory for multiple-pulse sequences, but to verify this theory by comparison with experimental results.

An important insight to this problem can be obtained by looking at the eigenenergies obtained for two nuclei under the quadrupole Hamiltonian, and the possible transitions afforded by both the rf pulses and dipolar interaction between nuclei. For a single spin-1 nucleus the possible quadrupolar levels are in $|0\rangle$, $|-\rangle \equiv \frac{|-1\rangle-|1\rangle}{\sqrt{2}}$, and $|+\rangle \equiv \frac{|1\rangle+|-1\rangle}{\sqrt{2}}$, where $|1\rangle$, $|0\rangle$, $|-1\rangle$ denote states having projections of nuclear spin along the z-axis of the principle axes (PAS) frame of the electric field gradient (EFG) centered at the nucleus. Radio frequency which creates transition between $|+\rangle$ and $|-\rangle$ is ω_z, between $|-\rangle$ and $|0\rangle$ is ω_y, and between $|0\rangle$ and $|+\rangle$ is ω_x.[10] In Fig. 1, we use ω_y rf to illustrate that the nine levels can always be broken down into two separate subsystems, plus a lone state, that are independent of one another. Each subsystem involves only four levels, so that instead of dealing with 9×9 matrices generally required for two spin-1 nuclei, one has 4×4 matrices. The 4×4 matrices lend themselves to the use of Dirac notation[11] in the following discussion. In particular, we choose to represent an operator S in the following manner:

$$S = S^W + S^V + |9\rangle\langle 9|S|9\rangle\langle 9|, \tag{1}$$

$$S^W = \sum_{i=1}^{4}\sum_{j=1}^{4} S(i,j)|i\rangle\langle j|, \tag{2}$$

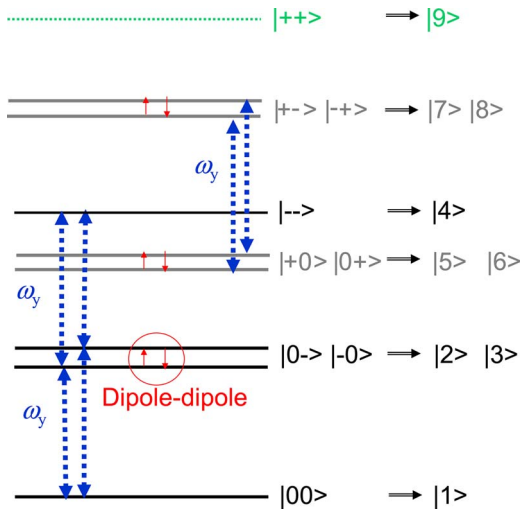

FIG. 1. (Color online) The energy levels for two nitrogen atoms are labeled using the notation $|ab\rangle$, corresponding to the two spins a and b each with one of the possible eigenstates of H_Q ($|0\rangle$, $|-\rangle$, or $|+\rangle$). The nonzero matrix elements of the dipolar Hamiltonian and the rf Hamiltonian in the interaction representation of the quadrupole Hamiltonian give the possible transitions. In the figure, the degenerate levels are separated to show the flip-flop terms of the dipolar Hamiltonian. The gray levels, or V-levels, form a subsystem isolated from the black levels, or W-levels.

$$S^V = \sum_{i=5}^{8}\sum_{j=5}^{8} S(i,j)|i\rangle\langle j|, \tag{3}$$

where levels $|1\rangle$ to $|9\rangle$ correspond to the nine levels shown in Fig. 1 and $S(i,j)$ are the matrix elements $\langle i|S|j\rangle$. Since both S^V and S^W are equivalent to 4×4 matrices, we will make use of the fact that they can also be represented by a sum of the 16 Dirac matrices. Using the notation of Ref. 11 for Dirac matrices $E_{k,l}=\rho_k\sigma_l$, we define two subsets of operators:

$$E^W_{k,l} = \sum_{i=1}^{4}\sum_{j=1}^{4} E_{k,l}(i,j)|i\rangle\langle j|, \tag{4}$$

operate *only* on the W-levels of Fig. 1 (eigenstates $|1\rangle$ through $|4\rangle$), and

$$E^V_{k,l} = \sum_{i=5}^{8}\sum_{j=5}^{8} E_{k,l}(i-4,j-4)|i\rangle\langle j|, \tag{5}$$

operate *only* on the V-levels of Fig. 1 (eigenstates $|5\rangle$ through $|8\rangle$).

For example, the quadrupole Hamiltonian H_Q can be rewritten as a sum of the above 32 operators found in Eqs. (4) and (5) and the lone operator $|9\rangle\langle9|$. We start with a general expression for H_Q,

$$\begin{aligned} H_Q = {} & 2\epsilon_0|1\rangle\langle1| + (\epsilon_0+\epsilon_-)(|2\rangle\langle2| + |3\rangle\langle3|) + 2\epsilon_-|4\rangle\langle4| \\ & + (\epsilon_0+\epsilon_+)(|5\rangle\langle5| + |6\rangle\langle6|) + (\epsilon_- + \epsilon_+)(|7\rangle\langle7| \\ & + |8\rangle\langle8|) + 2\epsilon_+|9\rangle\langle9|, \end{aligned} \tag{6}$$

where the eigenenergies are expressed in terms of those for a single atom, $\epsilon_\pm \equiv [V_{zz} \pm (V_{xx}-V_{yy})]\frac{eQ}{4}$ and $\epsilon_0 \equiv -\epsilon_+ - \epsilon_-$ for the nuclear quadrupole moment Q and the second derivatives of the electric potential V. We rewrite this as

$$H_Q = \frac{\hbar\omega_y}{2}(\rho_3^V + \sigma_3^W + \rho_3^W) + \frac{\epsilon_+}{2}(4|9\rangle\langle9| + E_{00}^V - 2E_{00}^W), \tag{7}$$

where $\hbar\omega_y \equiv \epsilon_0 - \epsilon_-$ and E_{00} is the 4×4 identity operator. By expressing H_Q in this way, we can easily identify the relevant part of H_Q. The identity operators and the lone operator can be ignored when the system starts from equilibrium, so that the effective H_Q is simply $\frac{\hbar\omega_y}{2}(\rho_3^V+\sigma_3^W+\rho_3^W)$. This effective Hamiltonian is derived for near-resonant ω_y excitation. Effective Hamiltonians for other excitation frequencies can easily be derived in a similar manner.

I. GENERAL SOLUTION

The density matrix ϱ describing the states of two spins, spin a and spin b, evolves under the total Hamiltonian which includes the quadrupole interaction H_Q, the dipole-dipole interaction H_d between two nitrogen atoms, and the applied rf pulses $H_{\rm rf}$. We assume that $0<|V_{xx}-V_{yy}|<|V_{zz}|$ and that the rf is applied close to ω_y, but not necessarily on resonance. The total Hamiltonian can be written as

$$H_{total} = H_d + H_{\rm rf} + U + H_0, \tag{8}$$

where $H_0 \equiv \frac{\omega_{\rm rf}}{\omega_y}H_Q$ and $U \equiv -\frac{\Delta\omega}{\omega_y}H_Q$ for $\Delta\omega \equiv \omega_{\rm rf}-\omega_y$. In general both H_Q and H_d are time dependent due to thermal molecular motion.[12] However, the theoretical inclusion of this motion is beyond the scope of this paper, and will be treated in a later study. We treat both H_Q and H_d as static. The density matrix evolves under the Liouville equation

$$-i\hbar\frac{d\varrho}{dt} = [\varrho, H_{total}] = [\varrho, H_d + H_{\rm rf} + U + H_0], \tag{9}$$

which in the interaction representation of H_0, where $\tilde{\varrho} \equiv e^{iH_0t/\hbar}\varrho e^{-iH_0t/\hbar}$, reduces to

$$-i\hbar\frac{d\tilde{\varrho}}{dt} = [\tilde{\varrho}, \tilde{H}_d + \tilde{H}_{\rm rf} + \tilde{U}]. \tag{10}$$

In the next paragraphs, we evaluate each of the three operators $\tilde{H}_d$, $\tilde{H}_{\rm rf}$, and $\tilde{U}$.

Working in the frame corresponding to the principle axes frame of V_{ij} centered at nucleus a with $|V_{zz}|>|V_{yy}|>|V_{xx}|$ (unprimed frame with unit vectors $\hat{x}$, $\hat{y}$, $\hat{z}$), the dipole Hamiltonian for spin-a and spin-b is

$$H_d/\hbar = \frac{\mu_0}{4\pi}\frac{\gamma^2\hbar}{r^3}[\mathbf{I}_a\cdot\mathbf{I}_b - 3(\mathbf{I}_a\cdot\hat{r})(\mathbf{I}_b\cdot\hat{r})], \tag{11}$$

where $\boldsymbol{r}$ is the radius vector from a to b, μ_0 is the permeability of free space, and γ is the gyromagnetic ratio. For ease of calculation, we wish to express $\mathbf{I}_b$ in the PAS frame of V_{ij} centered at nucleus-b (primed frame with unit vectors $\hat{x}'$, $\hat{y}'$, $\hat{z}'$):

$$\begin{pmatrix} I_{xb} \\ I_{yb} \\ I_{zb} \end{pmatrix} = \begin{pmatrix} \hat{x}\cdot\hat{x}' & \hat{x}\cdot\hat{y}' & \hat{x}\cdot\hat{z}' \\ \hat{y}\cdot\hat{x}' & \hat{y}\cdot\hat{y}' & \hat{y}\cdot\hat{z}' \\ \hat{z}\cdot\hat{x}' & \hat{z}\cdot\hat{y}' & \hat{z}\cdot\hat{z}' \end{pmatrix} \begin{pmatrix} I'_{xb} \\ I'_{yb} \\ I'_{zb} \end{pmatrix}. \tag{12}$$

The dipolar Hamiltonian becomes

$$H_d/\hbar = \sum_{i=xa,ya,za} \sum_{j=xb,yb,zb} \alpha_{ij} I_i I'_j. \tag{13}$$

If we expand the angular momentum operators in terms of the quadrupole eigenstates (for example, $I_{ya} = -i|-\rangle\langle 0| + i|0\rangle\langle -|$ operating on spin-a) and convert to the interaction representation, we find that only the flip-flop terms of Fig. 1 remain under the secular approximation,

$$\tilde{H}_d/\hbar = \sum\sum \alpha_{ij} e^{iH_0 t/\hbar} I_i I'_j e^{-iH_0 t/\hbar} \approx \alpha_{ya,yb}(|2\rangle\langle 3| + |3\rangle\langle 2|) + \alpha_{xa,xb}(|5\rangle\langle 6| + |6\rangle\langle 5|) + \alpha_{za,zb}(|7\rangle\langle 8| + |8\rangle\langle 7|). \tag{14}$$

In the above expression,

$$\alpha_{xa,xb} = \frac{\mu_0}{4\pi}\frac{\gamma^2\hbar}{r^3}[(1-3(\hat{x}\cdot\hat{r})^2)\hat{x}\cdot\hat{x}' - 3(\hat{x}\cdot\hat{r})(\hat{y}\cdot\hat{r})\hat{y}\cdot\hat{x}' - 3(\hat{x}\cdot\hat{r})(\hat{z}\cdot\hat{r})\hat{z}\cdot\hat{x}'],$$

$$\alpha_{ya,yb} = \frac{\mu_0}{4\pi}\frac{\gamma^2\hbar}{r^3}[(1-3(\hat{y}\cdot\hat{r})^2)\hat{y}\cdot\hat{y}' - 3(\hat{y}\cdot\hat{r})(\hat{x}\cdot\hat{r})\hat{x}\cdot\hat{y}' - 3(\hat{y}\cdot\hat{r})(\hat{z}\cdot\hat{r})\hat{z}\cdot\hat{y}'],$$

$$\alpha_{za,zb} = \frac{\mu_0}{4\pi}\frac{\gamma^2\hbar}{r^3}[(1-3(\hat{z}\cdot\hat{r})^2)\hat{z}\cdot\hat{z}' - 3(\hat{z}\cdot\hat{r})(\hat{x}\cdot\hat{r})\hat{x}\cdot\hat{z}' - 3(\hat{z}\cdot\hat{r})(\hat{y}\cdot\hat{r})\hat{y}\cdot\hat{z}']. \tag{15}$$

In addition, we can break up the dipolar Hamiltonian into two pieces, the first line of $\tilde{H}_d$ in Eq. (14) corresponds to the W-levels,

$$\tilde{H}_d^W/\hbar = \frac{\eta}{2\tau}(\rho_1^W\sigma_1^W + \rho_2^W\sigma_2^W), \tag{16}$$

and the second line of Eq. (14) to the V-levels,

$$\tilde{H}_d^V/\hbar = \frac{\zeta}{2\tau}\sigma_1^V + \frac{\xi}{2\tau}\sigma_1^V\rho_3^V, \tag{17}$$

where $\eta \equiv \alpha_{ya,yb}\tau$, $\zeta \equiv (\alpha_{za,zb} + \alpha_{xa,xb})\tau$, and $\xi \equiv (\alpha_{za,zb} - \alpha_{xa,xb})\tau$. As can easily be shown using the commutation relations of the Dirac matrices,[11] the three terms of the dipole Hamiltonian, with the coefficients η, ζ, and ξ, commute with one another.

We irradiate both nuclei with rf near ω_y with phase ϕ in the direction $\hat{rf}$, lasting for a time t_p, with field strength B,

$$\tilde{H}_{rf}/\hbar = -e^{iH_0 t_p/\hbar}\gamma B\cos(\omega_{rf}t_p - \phi)(\hat{y}\cdot\hat{rf}I_{ya} + y'\cdot\hat{rf}I'_{yb})e^{-iH_0 t_p/\hbar}. \tag{18}$$

In this expression we have anticipated that only the projection of rf on the y-axis of the spin-a PAS frame and the y' of the spin-b PAS will survive the secular approximation.[13] For evaluation of this expression, it is convenient to recognize that we can rewrite it in terms of a set of 12 operators, with four subsets, shown in Table I. The operators in one subset or row commute with any operator in another subset or row, and within a subset the operators are related to each other like fictitious spin-1/2 operators, e.g., $[I_1^{Wa}, I_2^{Wa}] = iI_3^{Wa}$. Therefore rewriting $H_0/\hbar = \omega_{\rm rf}(I_3^{Wa} + I_3^{Wb} + I_3^{Va} + I_3^{Vb})$, $I_{ya} = 2(I_2^{Wa} + I_2^{Va})$, and $I'_{yb} = 2(I_2^{Wb} + I_2^{Vb})$, we have

$$\tilde{H}_{rf}/\hbar = -2\gamma B\cos(\omega_{rf}t_p - \phi)\{(\hat{y}\cdot\hat{rf})[(I_2^{Wa} + I_2^{Va})\cos\omega_{rf}t_p + (I_1^{Wa} + I_1^{Va})\sin\omega_{rf}t_p] + (\hat{y}'\cdot\hat{rf})[(I_2^{Wb} + I_2^{Vb})\cos\omega_{rf}t_p + (I_1^{Wb} + I_1^{Vb})\sin\omega_{rf}t_p]\}. \tag{19}$$

Using the secular approximation to eliminate terms containing $2\omega_{rf}$, $\tilde{H}_{\rm rf}/\hbar$ reduces to

$$\tilde{H}_{rf}t_p/\hbar = -\theta_a(\cos\phi(I_2^{Wa} + I_2^{Va}) + \sin\phi(I_1^{Wa} + I_1^{Va})) - \theta_b(\cos\phi(I_2^{Wb} + I_2^{Vb}) + \sin\phi(I_1^{Wb} + I_1^{Vb})), \tag{20}$$

where $\theta_a \equiv (\hat{y}\cdot\hat{rf})\gamma B t_p$ and $\theta_b \equiv (\hat{y}'\cdot\hat{rf})\gamma B t_p$.

By its definition, U commutes with H_0, so that

$$\tilde{U}/\hbar = U/\hbar = -\frac{\Delta\omega}{2}(\rho_3^W + \sigma_3^W + \rho_3^V) = -\Delta\omega(I_3^{Wa} + I_3^{Wb} + I_3^{Va} + I_3^{Vb}). \tag{21}$$

For simplicity, we assume that the resonant off-set $\Delta\omega$ is the same for both the nuclei. This is tantamount to saying that the difference in resonant offset between two neighboring nuclei is much smaller than $\frac{1}{2\tau}$, where 2τ is the spacing between the refocusing pulses.

Having defined the evolution operators, we turn to the initial condition of the system in thermal equilibrium, where the reduced density matrix in thermal equilibrium is given by

$$\varrho_0 = -\frac{H_Q}{9kT} = -\frac{\hbar\omega_y}{9kT}(I_3^{Wa} + I_3^{Wb} + I_3^{Va} + I_3^{Vb}). \tag{22}$$

After the X-preparatory pulse [$\phi = 0$ in Eq. (20)], with frequency close to ω_y applied along the direction $\hat{rf}$ and lasting for a time t_0, the density matrix becomes

$$\tilde{\varrho}(t = t_0) = -\frac{\hbar\omega_y}{9kT}e^{-i(\tilde{H}_{rf}+U)t_0/\hbar}(\mathbf{I}^{Wa} + \mathbf{I}^{Wb} + \mathbf{I}^{Va} + \mathbf{I}^{Vb})\cdot\hat{k}e^{i(\tilde{H}_{rf}+U)t_0/\hbar}, \tag{23}$$

where we have neglected $\tilde{H}_d$ ($\tilde{H}_d \ll \tilde{H}_{rf}$). With any row of the fictitious spin-1/2 operators of Table I we have the general relationship[14]

$$e^{i\theta\mathbf{I}\cdot\mathbf{n}_r}\mathbf{I}\cdot\mathbf{n}_e e^{-i\theta\mathbf{I}\cdot\mathbf{n}_r} = \mathbf{I}\cdot[\cos\theta\mathbf{n}_e + \sin\theta(\mathbf{n}_e\times\mathbf{n}_r) + \mathbf{n}_e\cdot\mathbf{n}_r(1-\cos\theta)\mathbf{n}_r]. \tag{24}$$

TABLE I. Fictitious spin-1/2 angular momentum operators $\mathbf{I}=(I_1,I_2,I_3)$ corresponding to the axes $(\hat{i},\hat{j},\hat{k})$.

	Equivalent to I_1	Equivalent to I_2	Equivalent to I_3
$\boldsymbol{I}^{Wa}\equiv$	$\rho_1^W/2$	$\rho_2^W/2$	$\rho_3^W/2$
$\boldsymbol{I}^{Wb}\equiv$	$\sigma_1^W/2$	$\sigma_2^W/2$	$\sigma_3^W/2$
$\boldsymbol{I}^{Va}\equiv$	$\rho_1^V(1-\sigma_3^V)/4$	$\rho_2^V(1-\sigma_3^V)/4$	$\rho_3^V(1-\sigma_3^V)/4$
$\boldsymbol{I}^{Vb}\equiv$	$\rho_1^V(1+\sigma_3^V)/4$	$\rho_2^V(1+\sigma_3^V)/4$	$\rho_3^V(1+\sigma_3^V)/4$

Using this relationship, each of the four terms of Eq. (23) is evaluated separately. We recognize $\mathbf{n}_e=\hat{k}$ and the rotation due to the preparatory pulse for spin-a is $\theta\mathbf{n}_r=\theta_{0a}\hat{j}+\Delta\omega t_0\hat{k}$ where $\theta_{0a}\equiv(\hat{y}\cdot\hat{rf})\gamma B_0 t_0$ and similarly for spin-b with $\theta_{0b}\equiv(\hat{y}'\cdot\hat{rf})\gamma B_0 t_0$. Therefore Eq. (23) becomes

$$\begin{aligned}\tilde{\varrho}(t=t_0)=&\frac{-\hbar\omega_y}{9kT}(\boldsymbol{I}^{Wa}+\boldsymbol{I}^{Va})\cdot\left(\cos\theta'_{0a}\hat{k}-\sin\theta'_{0a}\hat{i}\frac{\theta_{0a}}{\theta'_a}\right.\\&\left.+\frac{\Delta\omega t_0}{\theta'_{0a}}(1-\cos\theta'_{0a})\frac{\theta_{0a}\hat{j}+\Delta\omega t_0\hat{k}}{\theta'_{0a}}\right)\\&+\frac{-\hbar\omega_y}{9kT}(\boldsymbol{I}^{Wb}+\boldsymbol{I}^{Vb})\cdot\left(\cos\theta'_{0b}\hat{k}-\sin\theta'_{0b}\hat{i}\frac{\theta_{0b}}{\theta'_{0b}}\right.\\&\left.+\frac{\Delta\omega t_0}{\theta'_{0b}}(1-\cos\theta'_{0b})\frac{\theta_{0b}\hat{j}+\Delta\omega t_0\hat{k}}{\theta'_{0b}}\right),\end{aligned}$$

where $\theta'_{0a}\equiv\sqrt{\theta_{0a}^2+\Delta\omega^2 t_0^2}$ and similarly for b. Experimentally we subtract successive experiments in which the signs of θ_{0a} and θ_{0b} have been inverted, in order to reduce interference and eliminate ringing effects from subsequent refocusing pulses. Using this same condition, the above expression reduces to

$$\begin{aligned}\tilde{\varrho}(t=t_0)=&\frac{\hbar\omega_y}{9kT}[\sin\theta'_{0a}(\boldsymbol{I}^{Wa}+\boldsymbol{I}^{Va})\cdot\mathbf{n}_{0a}\\&+\sin\theta'_{0b}(\boldsymbol{I}^{Wb}+\boldsymbol{I}^{Vb})\cdot\mathbf{n}_{0b}],\end{aligned}\tag{25}$$

where $\mathbf{n}_{0a}\equiv\frac{\theta_{0a}}{\theta'_{0a}}\left[\hat{i}-\frac{\Delta\omega t_0}{\theta'_{0a}}\frac{1-\cos\theta'_{0a}}{\sin\theta'_{0a}}\hat{j}\right]$ and similarly for $\mathbf{n}_{0b}$. Although $\mathbf{n}_{0a}$ and $\mathbf{n}_{0b}$ are not in general unit vectors, they approach $\hat{i}$ in the limit of a delta-function ($t_0=0$, θ=constant) preparatory pulse.

After the preparatory pulse, the general solution to $\tilde{\varrho}$ is

$$\tilde{\varrho}(t)=e^{-(i/\hbar)(\tilde{U}+\tilde{H}_{rf}+\tilde{H}_d)(t-t_0)}\tilde{\varrho}(t=t_0)e^{(i/\hbar)(\tilde{U}+\tilde{H}_{rf}+\tilde{H}_d)(t-t_0)}.\tag{26}$$

Again we assume that $\tilde{H}_d\ll\tilde{H}_{rf}$ so that when the rf is on $\tilde{U}+\tilde{H}_{rf}+\tilde{H}_d\approx\tilde{U}+\tilde{H}_{rf}$. When the rf is off $\tilde{U}+\tilde{H}_{rf}+\tilde{H}_d=\tilde{U}+\tilde{H}_d$. Since $\tilde{U}$ and $\tilde{H}_d$ commute, we can express Eq. (26) as

$$\tilde{\varrho}(t=2N\tau+Nt_r+t_0)=(DPD)^N\varrho(t=t_0)(DPD)^{\dagger N}\tag{27}$$

where

$$D\equiv e^{-(i/\hbar)\tilde{H}_d\tau},$$

$$P\equiv e^{-(i/\hbar)\tilde{U}\tau}e^{-(i/\hbar)(\tilde{H}_{rf}+\tilde{U})t_r}e^{-(i/\hbar)\tilde{U}\tau},\tag{28}$$

τ is the time between the preparatory pulse and the first refocusing pulse, N the number of pulses, and t_r is the refocusing pulse length. We apply Y refocusing pulses, or $\phi=\frac{\pi}{2}$ in Eq. (20).

The term P, representing three successive rotations as can be seen in Eq. (28), can easily be simplified to represent a single rotation using quaternions[14,15] and fictitious spin-1/2 operators of Table I. The three rotations can then be defined by rotation axes $\{\mathbf{n}_1,\mathbf{n}_2,\mathbf{n}_3\}$ and rotations $\{\theta_1,\theta_2,\theta_3\}$, where the second rotation depends on whether you are calculating the rotation for spin-a or spin-b,

$$\theta_1=\theta_3=\Delta\omega\tau,\tag{29}$$

$$\mathbf{n}_1=\mathbf{n}_3=\hat{k},$$

$$\begin{aligned}\theta_2=\theta'_a\equiv\sqrt{\theta_a^2+\Delta\omega^2 t_r^2}\ \text{or}\\=\theta'_b\equiv\sqrt{\theta_b^2+\Delta\omega^2 t_r^2},\end{aligned}\tag{30}$$

$$\begin{aligned}\mathbf{n}_2=\mathbf{n}_a\equiv\frac{\theta_a\hat{i}+\Delta\omega t_r\hat{k}}{\theta'_a}\ \text{or}\\=\mathbf{n}_b\equiv\frac{\theta_b\hat{i}+\Delta\omega t_r\hat{k}}{\theta'_b},\end{aligned}\tag{31}$$

where $\theta_a\equiv(\hat{y}\cdot\hat{rf})\gamma B_r t_r$ and $\theta_b\equiv(\hat{y}'\cdot\hat{rf})\gamma B_r t_r$.

The equivalent total rotation, θ_{tot} around $\mathbf{n}_{tot}$, can be found using the quaternion formalism for a time-symmetric triple rotation,[14,15]

$$\begin{aligned}\cos\frac{\theta_{tot}}{2}=&\cos\theta_1\cos\frac{\theta_2}{2}-\sin\theta_1\sin\frac{\theta_2}{2}\mathbf{n}_1\cdot\mathbf{n}_2,\\\sin\frac{\theta_{tot}}{2}\mathbf{n}_{tot}=&\sin\frac{\theta_2}{2}\mathbf{n}_2+2\sin\frac{\theta_1}{2}\mathbf{n}_1\\&\times\left(\cos\frac{\theta_1}{2}\cos\frac{\theta_2}{2}-\sin\frac{\theta_1}{2}\sin\frac{\theta_2}{2}\mathbf{n}_1\cdot\mathbf{n}_2\right).\end{aligned}\tag{32}$$

Using θ_{a-tot} for θ_{tot} with $\theta_2=\theta'_a$ and θ_{b-tot} for θ_{tot} with $\theta_2=\theta'_b$ and similarly for $\mathbf{n}_{tot}$, we can rewrite P as

$$P=e^{i\theta_{a-tot}\mathbf{I}^{Wa}\cdot\mathbf{n}_{a-tot}}e^{i\theta_{b-tot}\mathbf{I}^{Wb}\cdot\mathbf{n}_{b-tot}}e^{i\theta_{a-tot}\mathbf{I}^{Va}\cdot\mathbf{n}_{a-tot}}e^{i\theta_{b-tot}\mathbf{I}^{Vb}\cdot\mathbf{n}_{b-tot}}\tag{33}$$

using the fact that $\mathbf{I}^{Wa}$, $\mathbf{I}^{Wb}$, $\mathbf{I}^{Va}$, and $\mathbf{I}^{Vb}$ commute with one another. Further, we can expand each of the exponentials with the use of anticommutation and commutation identities of the Dirac matrices[11] to find

$$P = \left[\mathbf{1}^W \cos\frac{\theta_{a-tot}}{2} + 2i\mathbf{I}^{Wa}\cdot\mathbf{n}_{a-tot}\sin\frac{\theta_{a-tot}}{2} \right] \times \left[\mathbf{1}^W \cos\frac{\theta_{b-tot}}{2} + 2i\mathbf{I}^{Wb}\cdot\mathbf{n}_{b-tot}\sin\frac{\theta_{b-tot}}{2} \right]$$
$$\times \left[(\mathbf{1}^V + \sigma_3^V)/2 + (\mathbf{1}^V - \sigma_3^V)/2\cos\frac{\theta_{a-tot}}{2} + 2i\mathbf{I}^{Va}\cdot\mathbf{n}_{a-tot}\sin\frac{\theta_{a-tot}}{2} \right]$$
$$\times \left[(\mathbf{1}^V - \sigma_3^V)/2 + (\mathbf{1}^V + \sigma_3^V)/2\cos\frac{\theta_{b-tot}}{2} + 2i\mathbf{I}^{Vb}\cdot\mathbf{n}_{b-tot}\sin\frac{\theta_{b-tot}}{2} \right]. \quad (34)$$

In addition, because all three of the terms of Eqs. (16) and (17) for $\tilde{H}_d$ commute with one another, we can write

$$D \equiv e^{-(i/\hbar)\tilde{H}_d\tau} = e^{-i\eta(\rho_1^W\sigma_1^W+\rho_2^W\sigma_2^W)/2}e^{-i\zeta\sigma_1^V/2}e^{-i\xi\sigma_1^V\rho_3^V/2}$$
$$= [(\mathbf{1}^W + \rho_3^W\sigma_3^W)/2 + (\mathbf{1}^W - \rho_3^W\sigma_3^W)/2\cos\eta - i(\rho_1^W\sigma_1^W + \rho_2^W\sigma_2^W)/2\sin\eta]$$
$$\times \left[\cos\frac{\zeta}{2} - i\sigma_1^V\sin\frac{\zeta}{2}\right]\left[\cos\frac{\xi}{2} - i\sigma_1^V\rho_3^V\sin\frac{\xi}{2}\right]. \quad (35)$$

Complete expressions for DPD can be found in the Appendix.

Since the excitation coil is also used as the detection coil, the signal is proportional to the expectation value of the angular momentum operator $\boldsymbol{I}$ projected back onto the rf-direction

$$\langle \boldsymbol{I}\cdot\hat{rf}\rangle = \mathrm{Tr}\{\boldsymbol{I}\cdot\hat{rf}\varrho\} = \mathrm{Tr}\{e^{iH_0t}(\boldsymbol{I}\cdot\hat{rf})e^{-iH_0t}\bar{\varrho}\}, \quad (36)$$

where we have used the cyclic nature of the trace for square matrices. We further examine only signals that might arise near ω_y so that we replace $\boldsymbol{I}\cdot\hat{rf}$ by $(\hat{y}\cdot\hat{rf}I_{ya}+\hat{y}'\cdot\hat{rf}I'_{yb})$ in the expression above, which then simplifies to

$$\langle \boldsymbol{I}\cdot\hat{rf}\rangle = \frac{2}{\gamma B_r t_r}\mathrm{Tr}\{[\theta_a(\mathbf{I}^{Va}+\mathbf{I}^{Wa}) + \theta_b(\mathbf{I}^{Vb}+\mathbf{I}^{Wb})]\cdot\mathbf{n}_t\bar{\varrho}\}, \quad (37)$$

where $\mathbf{n}_t \equiv \sin\omega_{rf}t\hat{i} + \cos\omega_{rf}t\hat{j}$. An equivalent expression, useful in the next section, is

$$\langle \boldsymbol{I}\cdot\hat{rf}\rangle = \mathrm{Tr}\{[\sin\omega_{rf}t(\rho_1^V + \sigma_1^W + \rho_1^W) + \cos\omega_{rf}t(\rho_2^V + \sigma_2^W + \rho_2^W)]\theta_{avg}\bar{\varrho} + [\sin\omega_{rf}t(\rho_1^V\sigma_3^V + \sigma_1^W - \rho_1^W) + \cos\omega_{rf}t(\rho_2^V\sigma_3^V + \sigma_2^W - \rho_2^W)]\theta_{dif}\bar{\varrho}\}/(\gamma B_r t_r), \quad (38)$$

where

$$\theta_{avg} = \frac{\theta_b+\theta_a}{2} = \gamma B_r t_r\frac{\hat{y}'+\hat{y}}{2}\cdot\hat{rf} = \gamma B_r t_r\cos\frac{\theta_{EFG}}{2}\cos\theta_L,$$

$$\theta_{dif} = \frac{\theta_b-\theta_a}{2} = \gamma B_r t_r\frac{\hat{y}'-\hat{y}}{2}\cdot\hat{rf} = -\gamma B_r t_r\sin\frac{\theta_{EFG}}{2}\sin\theta_L\sin\phi_L. \quad (39)$$

In above expression θ_L and ϕ_L are defined with respect to the axes defined as $\hat{y}_{avg} = \frac{\hat{y}+\hat{y}'}{2\cos\frac{\theta_{EFG}}{2}}$ and $\hat{y}_{dif} = \frac{\hat{y}-\hat{y}'}{2\sin\frac{\theta_{EFG}}{2}}$ as shown in Fig. 2.

In order to calculate the observed signal for a powder one must average over all orientations of the EFG with respect to $\hat{rf}$

$$\langle \boldsymbol{I}\cdot\hat{rf}(2N\tau)\rangle_{avg} = \frac{1}{4\pi}\int_0^\pi\int_0^{2\pi}\langle \boldsymbol{I}\cdot\hat{rf}(2N\tau)\rangle\cos\theta_L d\theta_L d\phi_L. \quad (40)$$

II. ANALYTIC SOLUTIONS FOR DIPOLAR COUPLING ONLY

In order to understand the relative contribution of dipolar coupling and EFG inhomogeneity to the spin dynamics during the spin-lock spin-echo pulse sequence, we look separately at solutions involving only dipolar coupling and only EFG inhomogeneity. Starting with the dipolar coupling alone, we set $\Delta\omega=0$ and $U=0$ in the above expressions and are able to obtain analytic solutions for the echo size. We also define four subsets of operators, shown in Table II, which are closed under the operation of resonant Y-pulses

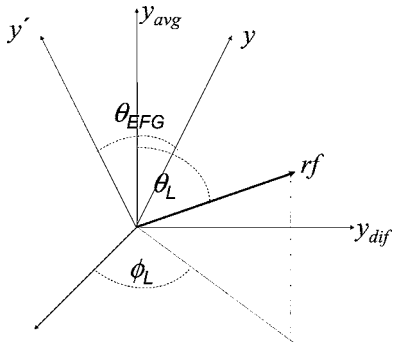

FIG. 2. The orientation of the rf excitation (θ_L, ϕ_L) with respect to the combined PAS frames of neighboring nuclei, defined by the average of the relevant axes $\hat{y}_{avg}$ and the difference $\hat{y}_{dif}$.

($\phi=\pi/2$) and dipolar coupling. The three operators in each subset are rotated within a three-dimensional space. We can represent these rotations using Pauli spin-matrices, much as was originally done by Cantor and Waugh.[10]

Using Eqs. (25) and (39), the density matrix after the preparatory pulse can be rewritten in terms of the operators of Table II,

$$\begin{aligned}\tilde{\varrho}(t=t_0) &= \frac{\hbar\omega_y}{18kT}[\sin\theta_{0avg}\cos\theta_{0dif}(\rho_1^V+\sigma_1^W+\rho_1^W)\\ &\quad+\sin\theta_{0dif}\cos\theta_{0avg}(\rho_1^V\sigma_3^V+\sigma_1^W-\rho_1^W)]\\ &= \frac{\hbar\omega_y}{9kT}[\sin\theta_{0avg}\cos\theta_{0dif}(A_1+A_3)\\ &\quad+\sin\theta_{0dif}\cos\theta_{0avg}(A_2+A_4)]. \qquad (41)\end{aligned}$$

Further, Eq. (20) simplifies, using Tables I and II, to

$$\begin{aligned}\tilde{H}_{rf}t_r/\hbar &= -\{(\rho_1^V+\sigma_1^W+\rho_1^W)\theta_{avg}+(\rho_1^V\sigma_3^V+\sigma_1^W-\rho_1^W)\theta_{dif}\}/2\\ &= -\{(A_1+A_3)\theta_{avg}+(A_2+A_4)\theta_{dif}\}. \qquad (42)\end{aligned}$$

The evolution of the density matrix in Eq. (41) under irradiation and dipolar coupling will generally result in an expression with all 12 of the operators of Table II. However, using the trace properties of the Dirac matrices,[11] it is easy to see from Eq. (38) that the only components which contribute to the signal are A_1, A_2, A_3, and A_4. Following the work of Cantor and Waugh, but with the operators defined in Table II, the effective density matrix after N pulses is

$$\begin{aligned}\tilde{\varrho}(2N\tau) &= \frac{\hbar\omega_y}{18kT}\Bigg\{\sin\theta_{0avg}\cos\theta_{0dif}\Bigg[g(N,\theta_{avg},\eta)(\sigma_1^W+\rho_1^W)\\ &\quad+g\left(N,\frac{\theta_{avg}}{2},\xi\right)\rho_1^V\Bigg]+\sin\theta_{0dif}\cos\theta_{0avg}\Bigg[g(N,\theta_{dif},\eta)\\ &\quad\times(\sigma_1^W-\rho_1^W)+g\left(N,\frac{\theta_{dif}}{2},\zeta\right)\rho_1^V\sigma_3\Bigg]\Bigg\}. \qquad (43)\end{aligned}$$

The function $g(N,\theta,p)$ is defined as

$$\left(1-2\sin^2\{N\cos^{-1}[\cos\theta\cos p]\}\frac{\cos^2\theta\sin^2 p}{1-\cos^2\theta\cos^2 p}\right),$$

where p is one of the three possible geometric parameters η, ξ, or ζ.

The expectation value of I from Eq. (38) is then

$$\langle \boldsymbol{I}\cdot\hat{rf}\rangle(2N\tau) = I_{avg}^W+I_{avg}^V+I_{dif}^W+I_{dif}^V \qquad (44)$$

$$\begin{aligned}&= \frac{2\hbar\omega_y}{3kT}\frac{1}{\gamma B_r t_r}\sin\omega_y t\Bigg\{\theta_{avg}\sin\theta_{0avg}\\ &\quad\times\cos\theta_{0dif}\left[\frac{2}{3}g(N,\theta_{avg},\eta)+\frac{1}{3}g\left(N,\frac{\theta_{avg}}{2},\xi\right)\right]\\ &\quad+\theta_{dif}\sin\theta_{0dif}\cos\theta_{0avg}\left[\frac{2}{3}g(N,\theta_{dif},\eta)\right.\\ &\quad\left.+\frac{1}{3}g\left(N,\frac{\theta_{dif}}{2},\zeta\right)\right]\Bigg\}, \qquad (45)\end{aligned}$$

where I_{avg}^W, I_{avg}^V, I_{dif}^W, and I_{dif}^V correspond to the four contributing terms of $\langle \boldsymbol{I}\cdot\hat{rf}(2N\tau)\rangle$ shown in the last equation above. One can see from Figs. 3(a) and 3(b) that $g(N,(2n+1)90^\circ,p)$ with integer n gives the maximum value and that for increasing dipolar coupling, represented by p, the average echo size for $\theta\neq(2n+1)90^\circ$ is smaller. When PAS frames for neighboring nuclei are misaligned, each of the four terms of Eq. (44) is maximized for four different refocusing pulses. When the PAS frames are aligned ($\theta_{\mathrm{dif}}=0$), the four terms collapse to two and we arrive at selective recoupling of two terms of the dipolar Hamiltonian. By observing the echo size as a function of the refocusing pulse strength, we can in principle determine at least two terms of the dipolar Hamiltonian. Combining this information with that of another transition, we then can find the full expression of the dipolar Hamiltonian, or the distance between neighboring nitrogen atoms.

TABLE II. Effect of propagators on select terms of the density matrix.

$\tilde{\varrho}$ component	Effect of P ($\phi=\pi/2$)	Effect of D
$A_1=\rho_1^V/2$	A_1	$A_1\cos\xi+B_1\sin\xi$
$B_1=\sigma_1^V\rho_2^V/2$	$B_1\cos\theta_{avg}-C_1\sin\theta_{avg}$	$B_1\cos\xi-A_1\sin\xi$
$C_1=\sigma_1^V\rho_3^V/2$	$C_1\cos\theta_{avg}+B_1\sin\theta_{avg}$	C_1
$A_2=\rho_1^V\sigma_3^V/2$	A_2	$A_2\cos\zeta+B_2\sin\zeta$
$B_2=-\rho_1^V\sigma_2^V/2$	$B_2\cos\theta_{dif}-C_2\sin\theta_{dif}$	$B_2\cos\zeta-A_2\sin\zeta$
$C_2=\sigma_1^V/2$	$C_2\cos\theta_{dif}+B_2\sin\theta_{dif}$	C_2
$A_3=(\sigma_1^W+\rho_1^W)/2$	A_3	$A_3\cos\eta+B_3\sin\eta$
$B_3=(-\rho_2^W\sigma_3^W-\rho_3^W\sigma_2^W)/2$	$B_3\cos 2\theta_{avg}-C_3\sin 2\theta_{avg}$	$B_3\cos\eta-A_3\sin\eta$
$C_3=(\rho_2^W\sigma_2^W-\rho_3^W\sigma_3^W)/2$	$C_3\cos 2\theta_{avg}+B_3\sin 2\theta_{avg}$	C_3
$A_4=(\sigma_1^W-\rho_1^W)/2$	A_4	$A_4\cos\eta+B_4\sin\eta$
$B_4=(\rho_3^W\sigma_2^W-\rho_2^W\sigma_3^W)/2$	$B_4\cos 2\theta_{dif}-C_4\sin 2\theta_{dif}$	$B_4\cos\eta-A_4\sin\eta$
$C_4=(\rho_2^W\sigma_2^W+\rho_3^W\sigma_3^W)/2$	$C_4\cos 2\theta_{dif}+B_4\sin 2\theta_{dif}$	C_4

Note that there is no decay associated with g as N increases, but a repetitive pattern evolves. In order for there to be decay over the echoes, the relative motion of the nuclei needs to be taken into account. This motion is beyond the scope of this paper, but is discussed in Refs. 7 and 12. Also experiments have verified that relaxation rate of the echoes, characterized by the time-constant T_{2e}, has a strong τ dependence, where for shorter τ, T_{2e} increases.[9,16]

In Figs. 3(c)–3(e), we model the effects of the four contributions in Eq. (44) to the average spin-echo from a powder sample for three different θ_{EFG}'s. It is clearly observable how the maxima and minima occur at increasing refocusing pulse strengths as θ_{EFG} increases. This effect is due to the reduction of effective tip angle by $\cos\frac{\theta_{EFG}}{2}$ or $\sin\frac{\theta_{EFG}}{2}$ as shown in Eq. (39).

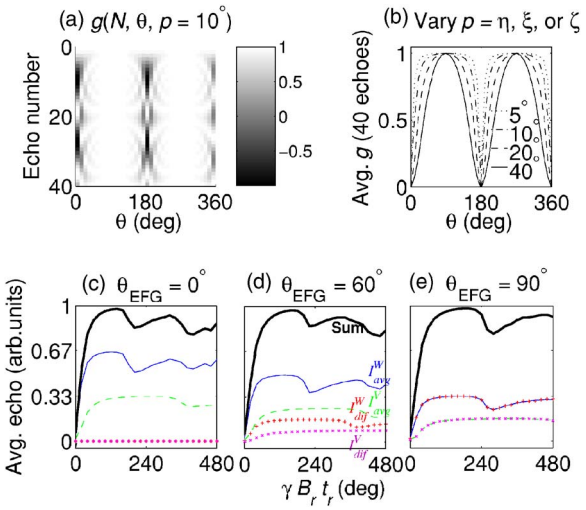

FIG. 3. (Color online) (a) The function $g(N,\theta,p)$ characteristic of the Nth echo size for an effective refocusing pulse θ in the presence of dipolar coupling and (b) how the average value of g increasingly deviates from unity for increasing dipolar coupling or p. (c)–(e) illustrate for a powder sample with $\eta=\xi=\zeta=10°$ the relative contributions to the average echo size for increasing dislocation between PAS frames of neighboring nuclei by θ_{EFG}. Notice how the maxima and minima occur at increasing refocusing pulse strengths as θ_{EFG} increases.

III. ANALYTIC SOLUTIONS FOR EFG INHOMOGENEITIES ONLY

We can also find an analytical expression for the echo size for the case of EFG inhomogeneity without any dipolar coupling. The evolution of the density matrix in the interaction representation without dipolar coupling reduces from Eq. (27) to

$$\tilde{\varrho}(t=2N\tau+Nt_r+t_0)=P^N\tilde{\varrho}(t=t_0)P^{\dagger N} \tag{46}$$

where, from Eq. (33),

$$P^N=e^{iN\theta_{a-tot}\mathbf{I}^{Wa}\cdot\mathbf{n}_{a-tot}}e^{iN\theta_{b-tot}\mathbf{I}^{Wb}\cdot\mathbf{n}_{b-tot}}e^{iN\theta_{a-tot}\mathbf{I}^{Va}\cdot\mathbf{n}_{a-tot}}\times e^{iN\theta_{b-tot}\mathbf{I}^{Vb}\cdot\mathbf{n}_{b-tot}}. \tag{47}$$

Using Eq. (37), we find after N pulses

$$\begin{aligned}\langle \boldsymbol{I}\cdot\hat{rf}\rangle=\frac{\hbar\omega_y}{3kT}\frac{1}{\gamma B_r t_r}\mathbf{n}_t\cdot\{&\theta_a\sin\theta'_{0a}[\cos N\theta_{a-tot}\mathbf{n}_{0a}\\&+(1-\cos N\theta_{a-tot})(\mathbf{n}_{0a}\cdot\mathbf{n}_{a-tot})\mathbf{n}_{a-tot}+\sin N\theta_{a-tot}\mathbf{n}_{0a}\\&\times\mathbf{n}_{a-tot}]+\theta_b\sin\theta'_{0b}[\cos N\theta_{b-tot}\mathbf{n}_{0b}\\&+(1-\cos N\theta_{b-tot})(\mathbf{n}_{0b}\cdot\mathbf{n}_{b-tot})\mathbf{n}_{b-tot}+\sin N\theta_{b-tot}\mathbf{n}_{0b}\\&\times\mathbf{n}_{b-tot}]\}.\end{aligned} \tag{48}$$

In the special case of delta-function pulses, $\tilde{\varrho}$ after the initial pulse is $\frac{\hbar\omega_y}{9kT}[\sin\theta_{0a}(\boldsymbol{I}^{Wa}+\boldsymbol{I}^{Va})\cdot\hat{i}+\sin\theta_{0b}(\boldsymbol{I}^{Wb}+\boldsymbol{I}^{Vb})\cdot\hat{i}]$. The rotation due to the refocusing pulse is determined by Eq. (32), noting that for delta-function pulses $\mathbf{n}_2=\hat{i}$,

$$\cos\frac{\theta_{tot}}{2}=\cos\theta_1\cos\frac{\theta_2}{2},$$

$$\sin\frac{\theta_{tot}}{2}\mathbf{n}_{tot}=\sin\frac{\theta_2}{2}\hat{i}+\sin\theta_1\cos\frac{\theta_2}{2}\hat{k}, \tag{49}$$

where here $\theta_1=\Delta\omega\tau$ and $\theta_2=\theta_a$ or θ_b. The evolution of the density matrix would be fixed or locked if the direction of net rotation corresponded to the direction of the initial magnetization or $\mathbf{n}_{tot}=\hat{i}$. This condition is fulfilled when $\theta_2=\pi$. Therefore this corresponds to the condition of maximum signal for a single crystal, as shown in Fig. 4(a). For a powder, the maximum signal occurs at about $\frac{4}{3}\pi$ as shown in Fig. 4(b).

As can be seen seen clearly from Eq. (49), the greatest deviation from the locked direction when $\theta_2\neq\pi$ occurs when $\theta_1=\Delta\omega\tau=\pi(n+\frac{1}{2})$, for integer n, or $\Delta f=\frac{1}{2\tau}(n+\frac{1}{2})$. The "dips" which occur for $\Delta f=\frac{1}{2\tau}(n+\frac{1}{2})$ are clearly shown in the theoretical curves of Fig. 4(c) for a single crystal and (d) for a powder. The above predictions were done for a linewidth of 150 Hz, much less than the dip spacing $(\frac{1}{2\tau})$. As the linewidth approaches $\frac{1}{2\tau}$ the dips will get smeared out or disappear; as the linewidth approaches zero the dips will reach their lowest values. Therefore the off-resonance behavior can be used as a measure of the contribution to the linewidth of EFG inhomogeneities.

IV. CALCULATING THE DIPOLAR PARAMETERS

The above calculations are done for a pair of spins. Although it is an intractable problem to determine the precise evolution of a large number of spins under the effect of dipolar coupling, we can approximate the effect of a number of nearby nuclei on a given nuclei by considering the second moment as a measure of their effect. The expression from Vega[17] for the second moment in NQR,

$$\hbar^2\langle\Delta\omega^2\rangle=\sum_k\frac{1}{3}\left(\frac{\theta_{dif}^2}{\theta_{dif}^2+\theta_{avg}^2}\right)\frac{\xi_{ik}^2}{\tau^2}+\frac{1}{3}\left(\frac{\theta_{avg}^2}{\theta_{dif}^2+\theta_{avg}^2}\right)\frac{\xi_{ik}^2}{\tau^2}+\frac{2}{3}\frac{\eta^2}{\tau^2}, \tag{50}$$

reveals that contributions to the linewidths add in quadrature for η, ζ, and ξ. Therefore we take in the above expression for η, $\eta_{eff}=\sqrt{\Sigma_k\eta_{ik}^2}$, and similarly for ζ and ξ.

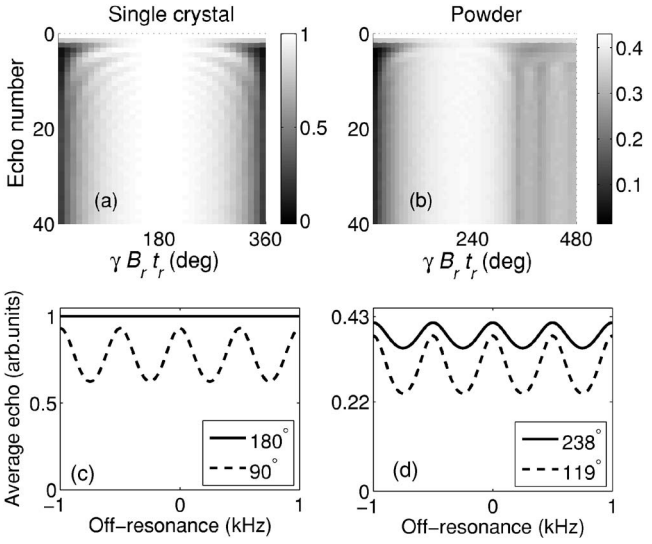

FIG. 4. Considering only EFGs and delta-function pulses (a) for a single crystal and (b) for a powder sample, shows the Nth echo size (units of $\frac{2\hbar\omega_y}{3kT}$), for a Gaussian linewidth (full width at half maximum=150 Hz) and τ=1 ms as a function of the refocusing pulse strength. (c) for a single crystal and (d) for a powder sample shows how the average signal size (for 40 echoes) varies little as a function of off-resonance for the optimal refocusing pulse, but quite significantly for refocusing pulses of half that value.

We calculated η_{eff}, ζ_{eff}, and ξ_{eff} for the two samples that were studied (distances for *p*-chloroaniline come from Ref. 18, and for sodium nitrite from Refs. 19–21). In the computational results shown in Table II all nuclei within a sphere of radius $4d$, where d is the largest length of the unit cell, were considered. All numerical values in Table III are in Hz. For all the transitions of sodium nitrite and for the ω_x transition of *p*-chloroaniline the nearest neighbors have the relevant axes aligned. However, the other two transitions of *p*-chloroaniline have neighboring nitrogen with relevant axes 65° degrees apart.[22,23] For these transitions, as shown in Table III, these unaligned neighboring nitrogens dominate the dipolar coupling, as opposed to those nitrogens which are further away but are aligned (last column).

V. EXPERIMENTAL RESULTS

All experiments were carried out at room temperature. The sodium nitrite sample consisted of 0.7 kg of $NaNO_2$, (97+% purity, Aldrich) mixed with oil to give a final volume of roughly 1 l. Mixing with oil is known to reduce piezoelectric effects due to coupling of the rf fields with the ferroelectric phase. The *p*-chloroaniline sample consisted of 1 kg of C_6H_6ClN, (98% purity, Aldrich) in a volume of roughly 1 l.

All experiments were carried out using Tecmag-based spectrometers (Tecmag, Houston, TX).[29] A homebuilt probe with a coil of volume of 1.5 l was used and tuned to the various NQR frequencies. The quality factor was typically 100 or less and the rf input power was 400 W or less.

In our experiments we acquired echoes for arrayed sets of SLSE sequences where the pulse lengths were held fixed and the rf power of either the initial pulse or the refocusing pulses was arrayed. To compensate for possible variations in sample temperature during the course of an experiment, which can lead to changes in line position and linewidth, a single complete scan contained both a series of SLSE echo trains with varying initial pulse and a series of SLSE echo trains with varying refocusing pulses. Typically 16 total scans were performed with a wait time between SLSE echo trains on the order of 1 s, at least 3 to 4 times the spin-lattice relaxation time for the transition under investigation.

The linewidth of the ω_z transition for sodium nitrite was measured to be 140 Hz full width at half maximum, corresponding to a variance $\Delta f_{rms}=\sqrt{\langle\Delta\omega^2\rangle}/(2\pi)$ of 60 Hz. The variance, according to Eq. (50) and Table III, for dipolar coupling alone would by 44 Hz. Therefore this sample provides a good demonstration of the effects of refocusing pulses in the regime where dipolar coupling contributes substantially to the linewidth. As shown in Fig. 5, the magnitude of the first echo signal as a function of refocusing pulse length differs substantially from later echoes. In particular two maxima, one for a refocusing pulse of ~150° and another for a refocusing pulse of ~290° become apparent, corresponding to the two maxima seen clearly in Fig. 3 with the solid black line. The theoretical predictions and the experimental data agree well, with small discrepancies. A possible cause for the discrepancies is the naive use in the theoretical model of a single T_{2e}. The value used corresponded to the experimental value for a 150° refocusing pulse (88 ms). However, as measured experimentally, the T_{2e} varied, from 0.64 to 1.27 of the value used in the theoretical model, as a function of the refocusing pulse (roughly mimicking the data). This interesting variation deserves further investigation.

TABLE III. Dipolar parameters expressed in Hz and calculated for *p*-chloroaniline and sodium nitrite.

	Expression			Sodium nitrite			*p*-chloroaniline-∠			*p*-chloroaniline-∥		
	$\frac{\zeta_{eff}}{\tau}$	$\frac{\xi_{eff}}{\tau}$	$\frac{\eta_{eff}}{\tau}$	$\frac{\zeta_{eff}}{2\pi\tau}$	$\frac{\xi_{eff}}{2\pi\tau}$	$\frac{\eta_{eff}}{2\pi\tau}$	$\frac{\zeta_{eff}}{2\pi\tau}$	$\frac{\xi_{eff}}{2\pi\tau}$	$\frac{\eta_{eff}}{2\pi\tau}$	$\frac{\zeta_{eff}}{2\pi\tau}$	$\frac{\xi_{eff}}{2\pi\tau}$	$\frac{\eta_{eff}}{2\pi\tau}$
ω_x	$\alpha_{yi,yk}+\alpha_{zi,zk}$	$\alpha_{yi,yk}-\alpha_{zi,zk}$	$\alpha_{xi,xk}$	26	66	26				7	25	12
ω_y	$\alpha_{zi,zk}+\alpha_{xi,xk}$	$\alpha_{zi,zk}-\alpha_{xi,xk}$	$\alpha_{yi,yk}$	43	29	43	7	24	10	5	8	5
ω_z	$\alpha_{xi,xk}+\alpha_{yi,yk}$	$\alpha_{xi,xk}-\alpha_{yi,yk}$	$\alpha_{zi,zk}$	26	66	26	20	7	14	4	10	4

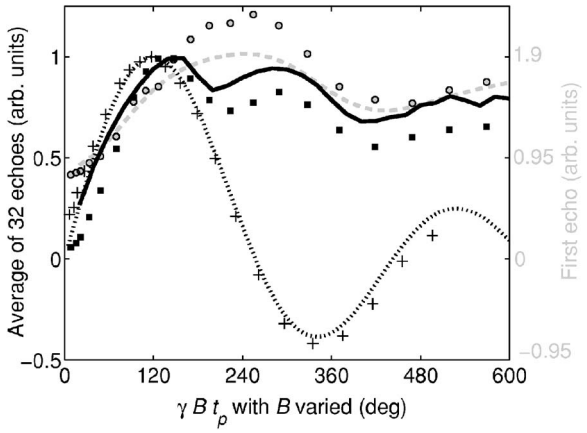

FIG. 5. For sodium nitrite, irradiated at ω_z (1.038 MHz) and using an optimum preparatory pulse of 119°, the signal from the first echo (theory in gray dashed line, experiment in gray circles) is compared to the average echo of 32 (theory in black solid line, experiment in black squares) as a function of refocusing pulse strength. The double peak of the averaged data is characteristic of a sample whose linewidth is dominated by dipolar coupling. For an optimal refocusing pulse of 150°, we also varied the preparatory pulse strength (theory in black dotted line, experiment in crosses). For all cases, τ=1.9 ms, pulse durations are t_0=120 μs and t_r =150 μs, and signals are normalized with respect to the optimal average echo.

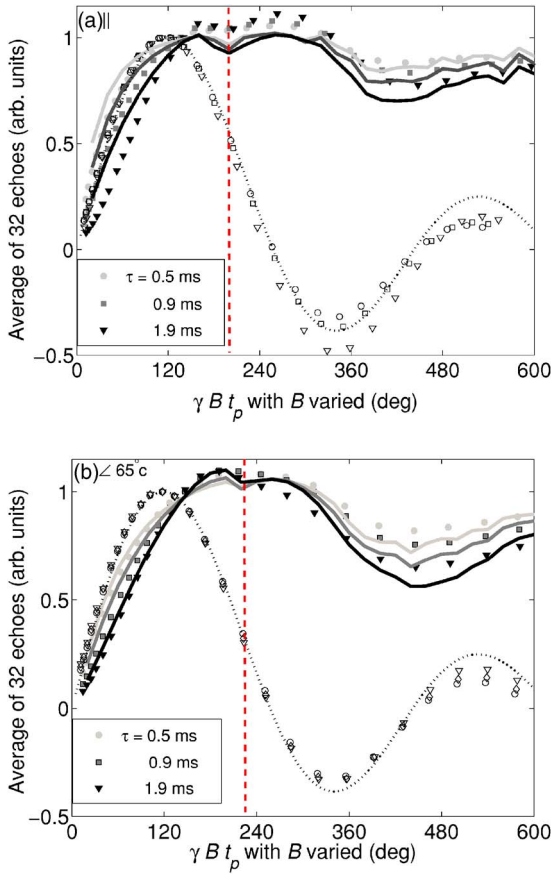

FIG. 6. (Color online) For *p*-chloroaniline irradiated at (a) ω_x (3.263 MHz) or (b) ω_y (2.767 MHz), using an optimum preparatory pulse of 119°, the average of 32 echoes varies as a function of pulse spacing τ and as a function of the refocusing pulse strength (theory in solid lines, experiments in filled symbols). The field strength was calibrated by fixing the refocusing pulse at 150° and varying the preparatory pulse (theory in dotted lines, experiments in open symbols). Pulse durations were t_0=160 μs and t_r=200 μs and signals for different τ's are shown normalized to their respective calibration curves.

The *B*-field for Fig. 5 was calibrated by varying the field strength for the preparatory pulse and keeping the refocusing pulse fixed ($\gamma B_r t_r 180°/\pi \approx 150°$). The experimental results for these scans are shown as crosses in Fig. 5 (the *x*-axis for this data refers to the strength of the preparatory pulse). By comparing the experimental results to the standard 3/2 Bessel function given first by Vega[24] (shown as the dotted line in the figure), we calibrated the experimental *B*-field in reference to the voltage from a small sniffer coil placed near the resonant circuit. Although the Bessel function was originally derived for the expected signal from a *single* pulse, our theoretical predictions for the signal response to a SLSE sequence, where the refocusing pulse is close to optimal, reveals a dependency on the preparatory pulse strength very close to that of the 3/2 Bessel function.

The second sample we examined, *p*-chloroaniline, differs substantially from sodium nitrite in two ways: (i) neighboring nitrogen do not have aligned PAS frames and (ii) the linewidths are dominated by EFG inhomogeniety (the variance for dipolar coupling alone is between 16 and 17 Hz, while the measured variance was 3–8 times larger, depending on the transition and the temperature of the sample). In particular the $\hat{y}$ axes of the PAS for neighboring nitrogen in *p*-chloroaniline are separated by 65°, while the $\hat{x}$ axes are aligned. Since the ω_x transition corresponds to the excitation projected onto the $\hat{x}$ axes and the ω_y transition to the $\hat{y}$ axes, we measured the response to a SLSE sequence for both transitions. Figure 6 shows the signal as a function of the refocusing pulse strength (corresponding to the solid lines and filled-in symbols), where the strength had been varied by changing the strength of the *B*-field. The *B*-field for the *p*-chloroaniline probe was calibrated in a similar manner to the sodium nitrite, and the relevant curves are shown as open symbols in Fig. 6.

Despite the small contribution of the dipole coupling to the overall linewidth, one can still see the effect of the dipolar parameters on some of the features of these graphs. For instance, one can see that the very shallow dip, denoted by the vertical dashed lines in both Figs. 6(a) and 6(b), occurs at about a 19%, or $1/\cos(65°/2)$, larger refocusing pulse for the ω_y transition than for the ω_x transition. The underlying cause for this shift is the 65° separation in the $\hat{y}$ axes of neighboring nitrogen compared to the aligned $\hat{y}$ axes.

We also varied the pulse-spacing for *p*-chloroaniline. The effect of changing the pulse spacing is twofold. One effect, which is accurately predicted by the theory, demonstrates that with increased pulsed spacing comes increased evolution during the time between pulses and a corresponding decrease

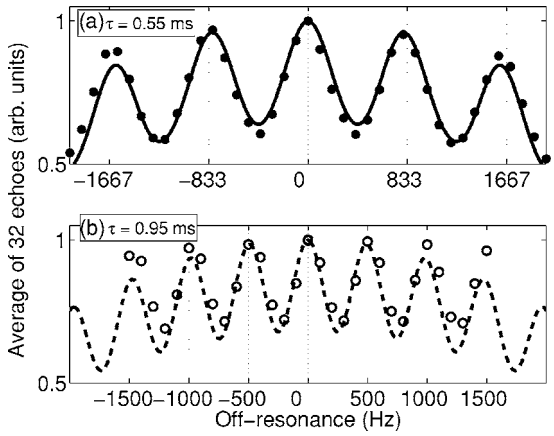

FIG. 7. For a sample of *p*-chloroaniline, irradiated at ω_y, as a function of off-resonance $[\Delta\omega/(2\pi)]$ for two different pulse spacing. Theory is shown as lines and the data as symbols, with the grid lines spaced at $1/(2\tau+t_r)$ to correspond to the predicted maxima. An optimum preparatory pulse of 119° and a refocusing pulse of 150° was used with pulse durations of $t_0=80$ μs and $t_r=100$ μs.

in the ability of nonoptimal refocusing pulses to refocus the evolution. This is seen clearly in Figs. 6(a) and 6(b) and in Fig. 3(b), by a decrease in signal for nonoptimal pulses. A second effect, not predicted by our two-spin model, is the dependence of T_{2e} on both the pulse spacing and the refocusing pulse length. For example, T_{2e} for the optimal refocusing pulse, varies for ω_x from 43 ms for $\tau=1.9$ ms to 60 ms for $\tau=0.5$ ms and for ω_y from 36 ms for $\tau=1.9$ ms to 47 ms for $\tau=0.5$ ms. The T_{2e}'s dependence on the refocusing pulse roughly mimics the data shown, so that the weaker refocusing pulses have shorter T_{2e}'s by as much as a factor of 2 from the optimal value. Again these variations are of interest and will be explored in a later paper.

In order to underscore the effect of the EFG inhomogeneity on the ability of rf pulses to refocus the signal, we examined the echo signal as a function of off-resonance for the ω_y transition of *p*-chloroaniline. The results for the SLSE sequence $119^\circ_X-(\tau-150^\circ_Y-\tau)_{N=32}$ are shown in Fig. 7, where the gridlines are spaced at $1/(2\tau+t_r)$ to denote where maxima are predicted to be. Similar "dips" have also been observed in other multiple-pulse NQR sequences.[25–28] These dips illustrate that even when the linewidth is centered on the rf frequency, the larger the linewidth, the more part of the line must be in one of the valleys, and the greater the overall degradation of the echo size becomes. This is particulary true as the linewidth approaches $1/(2\tau+t_r)$.

It is also clear from Fig. 7 that for increasing off-resonance there is an overall decrease in signal aside from the "dips." This decrease is caused by off-resonance during the pulse changing the net direction of rotation during the pulse. For example, the B-field used in these off-resonance experiments corresponds to $\gamma B_r/(2\pi)=4.1$ kHz, so that with an off-resonance of 2 kHz the angle of rotation has now been tipped away from its most effective direction by 26°.

CONCLUSIONS

The response of a system to a SLSE sequence, including the optimum refocusing pulse, has been shown, both experimentally and theoretically, to depend strongly on both the dipolar coupling and EFG inhomogeneity. When the linewidth is dominated by EFG inhomogeneity, the optimum refocusing pulse is $\gamma B_r t_r=\pi$ for a single crystal and approximately $\frac{4}{3}\pi$ for a powder sample. In contrast, when the linewidth is dominated by dipolar coupling, we have selective refocusing, where one component of the dipolar Hamiltonian is refocused for $\gamma B_r t_r=\pi$ and another component is refocused for $\frac{\pi}{2}$. Since twice as much of the signal is effected by the latter dipolar component than the former, the optimum refocusing pulse is slightly larger than $\frac{\pi}{2}$ for a single crystal and slightly larger than $\frac{4}{3}\frac{\pi}{2}$ for a powder sample. The exact maximum is determined by the precise orientation between neighboring nuclei. When the PAS frames are misaligned, the optimum refocusing pulse is pushed towards larger values, increasing approximately as $1/\cos(\theta_{EFG}/2)$. Further we have given general expressions for a sample with significant contributions from dipolar coupling *and* EFG inhomogeneity and found these theoretical predictions match well with experimental results. The results given here can serve not only to optimize the spin-lock spin-echo sequence for substance detection, but also to understand other multiple-pulse sequences in NQR.

ACKNOWLEDGMENTS

This work was supported by ONR and NSF.

APPENDIX

The general expression for $DPD=D^V P^V D^V+D^W P^W D^W$ is given by

$$D^V P^V D^V = \begin{pmatrix} e^{i\Delta\omega\tau}(c_\varsigma^2 C_b - s_\varsigma^2 C_a) & -ic_\varsigma e^{i\Delta\omega\tau} s_\varsigma (C_b + C_a) & -i(-c_\varsigma S_b c_\delta + s_\varsigma S_a s_\delta) & c_\varsigma S_b s_\delta + s_\varsigma S_a c_\delta \\ -ic_\varsigma e^{i\Delta\omega\tau} s_\varsigma (C_b + C_a) & -e^{i\Delta\omega\tau}(s_\varsigma^2 C_b - C_a c_\varsigma^2) & s_\varsigma S_b c_\delta + c_\varsigma S_a s_\delta & -i(s_\varsigma S_b s_\delta - c_\varsigma S_a c_\delta) \\ -i(-c_\varsigma S_b c_\delta + s_\varsigma S_a s_\delta) & s_\varsigma S_b c_\delta + c_\varsigma S_a s_\delta & e^{-i\Delta\omega\tau}(c_\delta^2 C_b^* - s_\delta^2 C_a^*) & -ic_\delta e^{-i\Delta\omega\tau} s_\delta (C_b^* + C_a^*) \\ c_\varsigma S_b s_\delta + s_\varsigma S_a c_\delta & -i(s_\varsigma S_b s_\delta - c_\varsigma S_a c_\delta) & -ic_\delta e^{-i\Delta\omega\tau} s_\delta (C_b^* + C_a^*) & e^{-i\Delta\omega\tau}(-s_\delta^2 C_b^* + c_\delta^2 C_a^*) \end{pmatrix}$$

and

$$D^W P^W D^W = \begin{pmatrix} a_{11} & a_{12} & a_{13} & a_{14} \\ a_{21} & a_{22} & a_{23} & a_{24} \\ a_{31} & a_{32} & a_{33} & a_{34} \\ a_{41} & a_{42} & a_{43} & a_{44} \end{pmatrix},$$

where

$$a_{11} = a_{44}^* = e^{i2\Delta\omega\tau} C_a C_b, \tag{A1}$$

$$a_{12} = a_{21} = e^{i\Delta\omega\tau}(ic_\eta C_a S_b + s_\eta S_a C_b), \tag{A2}$$

$$a_{13} = a_{31} = e^{i\Delta\omega\tau}(s_\eta C_a S_b + ic_\eta S_a C_b), \tag{A3}$$

$$a_{14} = a_{41} = -S_a S_b, \tag{A4}$$

$$a_{22} = -s_\eta^2 C_a^* C_b + (2is_\eta S_a S_b + c_\eta C_a C_b^*) c_\eta, \tag{A5}$$

$$a_{23} = a_{32} = s_\eta^2 S_a S_b + [(-iC_a C_b^* - iC_a^* C_b) s_\eta - c_\eta S_a S_b] c_\eta, \tag{A6}$$

$$a_{24} = a_{42} = (ic_\eta S_a C_b^* + s_\eta C_a^* S_b) e^{-i\Delta\omega\tau}, \tag{A7}$$

$$a_{33} = -s_\eta^2 C_a C_b^* + (2is_\eta S_a S_b + c_\eta C_a^* C_b) c_\eta, \tag{A8}$$

$$a_{34} = a_{43} = e^{-i\Delta\omega\tau}(s_\eta S_a C_b^* + ic_\eta C_a^* S_b). \tag{A9}$$

In the above expressions, the following definitions apply:

$$\varsigma \equiv \frac{\zeta + \xi}{2},$$

$$\delta \equiv \frac{\zeta - \xi}{2},$$

$$c_\chi \equiv \cos(\chi),$$

$$s_\chi \equiv \sin(\chi),$$

$$S_\chi \equiv \sin\left(\frac{\sqrt{\theta_\chi^2 + \Delta\omega^2 t_r^2}}{2}\right) \frac{\theta_\chi}{\sqrt{\theta_\chi^2 + \Delta\omega^2 t_r^2}},$$

$$C_\chi \equiv \cos\left(\frac{\sqrt{\theta_\chi^2 + \Delta\omega^2 t_r^2}}{2}\right) + i\frac{\Delta\omega t_r}{\sqrt{\theta_\chi^2 + \Delta\omega^2 t_r^2}} \sin\left(\frac{\sqrt{\theta_\chi^2 + \Delta\omega^2 t_r^2}}{2}\right).$$

Notice that C_χ reduces to $\cos(\theta_\chi/2)$ and S_χ reduces to $\sin(\theta_\chi/2)$ for $\Delta\omega t_r \ll \theta_\chi$.

*Also at Code 6122, Naval Research Laboratory, Washington, D.C. 20375, USA. Electronic address: ksauer@physics.gmu.edu

[1] A. N. Garroway, M. L. Buess, J. B. Miller, B. H. Suits, A. D. Hibbs, G. A. Barrall, R. Matthews, and L. J. Burnett, IEEE Trans. Geosci. Remote Sens. **39**, 1108 (2001).
[2] D. Y. Osokin, Phys. Status Solidi B **102**, 681 (1980).
[3] D. Y. Osokin, J. Mol. Struct. **83**, 243 (1982).
[4] O. S. Zueva and A. R. Kessel, J. Mol. Struct. **83**, 383 (1982).
[5] V. Mikhaltsevitch and T. Rudakov, Solid State Nucl. Magn. Reson. **25**, 99 (2004).
[6] M. M. Maricq, Phys. Rev. B **33**, 4501 (1986).
[7] G. E. Karnaukh, B. N. Provotorov, and A. K. Khitrin, Zh. Eksp. Teor. Fiz. **84**, 161 (1983).
[8] E. D. Ostroff and J. S. Waugh, Phys. Rev. Lett. **16**, 1097 (1966).
[9] R. A. Marino and S. M. Klainer, J. Chem. Phys. **67**, 3388 (1977).
[10] R. Cantor and J. Waugh, J. Chem. Phys. **73**, 1054 (1980).
[11] E. Weisstein, *Dirac Matrices (http://mathworld. wolfram. com/ DiracMatrices. html)* (Wolfram Research, Inc., Champaign, IL, 2005).
[12] N. A. Sergeev, A. M. Panich, and M. Olszewski, Appl. Magn. Reson. **27**, 41 (2004).
[13] Y. K. Lee, Concepts Magn. Reson. **14**, 155 (2002).
[14] K. L. Sauer, C. A. Klug, J. B. Miller, and A. N. Garroway, Appl. Magn. Reson. **25**, 485 (2004).
[15] C. Counsell, M. H. Levitt, and R. R. Ernst, J. Magn. Reson. (1969-1992) **63**, 133 (1985).
[16] V. Mikhaltsevitch and T. Rudakov, Phys. Status Solidi B **241**, 411 (2004).
[17] S. Vega, Adv. Magn. Reson. **6**, 259 (1973).
[18] G. Ploug-Sorensen and E. K. Andersen, Acta Crystallogr., Sect. C: Cryst. Struct. Commun. **C41**, 613 (1985).
[19] R. A. Marino and P. J. Bray, J. Chem. Phys. **48**, 4833 (1968).
[20] M. R. Truter, Acta Crystallogr. **7**, 73 (1954).
[21] G. B. Carpenter, Acta Crystallogr. **5**, 132 (1952).
[22] S. Vega, J. Chem. Phys. **63**, 3769 (1975).
[23] R. Ambrosetti, A. Colligiani, P. Grigolini, and F. Salvetti, J. Chem. Phys. **60**, 459 (1974).
[24] S. Vega, J. Chem. Phys. **61**, 1093 (1974).
[25] S. S. Kim, J. R. P. Jayakody, and R. A. Marino, Z. Naturforsch., A: Phys. Sci. **47**, 415 (1992).
[26] D. Y. Osokin, V. L. Ermakov, R. H. Kurbanov, and V. A. Shagalov, Z. Naturforsch., A: Phys. Sci. **47**, 439 (1992).
[27] T. N. Rudakov, V. T. Mikhaltsevich, and O. P. Selchikhin, J. Phys. D **30**, 1377 (1997).
[28] T. N. Rudakov and A. V. Belyakov, J. Phys. D **31**, 1251 (1998).
[29] Reference to this and other commercial products is for completeness, but products from other manufacturers could also be suitable.